

# On wall modeling for LES of particle-laden turbulent channel flows

By M. Bassenne, P. L. Johnson, J. Urzay AND P. Moin

## 1. Motivation and objectives

The direct numerical simulation (DNS) of all spatiotemporal scales encountered in industrial and environmental turbulent flows is often computationally untractable. The stringent numerical resolution required in DNS is partly alleviated in large-eddy simulations (LES). In LES, the dynamics of the energy-dominant eddies are resolved on a coarse computational mesh, while the effect of the unresolved subgrid-scale (SGS) motion is modeled (Sagaut 2006). When an appropriate SGS model is used, an LES solution is sufficient to predict the statistics that primarily depend on the dynamics of the large flow features. However, the prediction of processes that strongly depend on small-scale dynamics becomes more challenging, since increased weight is put onto the SGS model.

Particle-laden turbulence is an example of flows where the small scales play an important role, since the dispersed-phase dynamics are primarily governed by velocity gradients. In order to resolve these dynamics faithfully, the constraint of resolving the energy-dominant velocity gradient features would require computational grids that approach the DNS limit (Johnson & Meneveau 2018). The numerical grid employed in practical LES does not typically satisfy these requirements, which can lead to inaccurate predictions of the disperse- and carrier-phase statistics in regimes where the particles predominantly interact with small-scale eddies (Urzay *et al.* 2014). In particular, the preferential concentration phenomenon by which particles preferentially sample particular regions of the flow and form inhomogeneous spatial distributions is challenging to accurately predict in LES (Marchioli 2017).

Another exception to the earlier statement that coarse meshes allow for accurate solutions since large-scale energy-dominant eddies contribute most to the global dynamics is also found in wall-bounded flows. The size of the dominant flow structures near solid boundaries scales with the viscous length rather than the boundary-layer thickness. As the Reynolds number increases, the near-wall structures decrease in size relative to the boundary-layer thickness, resulting in prohibitive resolution requirements near the wall if the near-wall eddies ought to be resolved. LES of wall-bounded flows can be either wall-resolved (WRLES) or wall-modeled (WMLES) depending on whether the near-wall eddies are resolved or modeled on the computational grid, respectively. This is in contrast with DNS, which would resolve all flow length scales everywhere. The number of grid points necessary for DNS, WRLES, and WMLES of wall-bounded flows has been estimated in the literature (Chapman 1979; Choi & Moin 2012). The computational cost of WRLES scales near-quadratically as  $Re^{13/7}$ , where  $Re$  is the characteristic Reynolds number. Despite an improvement compared to the  $Re^{37/14}$  scaling required in DNS, it is still prohibitively expensive for a number of practical applications. In turn, the grid-point requirement for WMLES scales as  $Re$ , rendering it an attractive modeling strategy. However, when the resolution is coarsened near the wall in WMLES, the wall-shear stress cannot be trivially obtained from differencing the velocity profile, since the near-wall

solution is unknown. Instead, particular wall-modeling strategies need to be employed in the first cell to provide a better estimate of the wall-shear stress. The reader is referred to Bose & Park (2018) for a review.

Numerous efforts have been dedicated to the development of wall models for LES of wall-bounded turbulent flows, mainly focused so far on the prediction of single-phase statistics. As predictive wall models have emerged in this context, their assessment in more multiphysics scenarios is required. Of particular interest to the present study is the predictive capability of off-the-shelf WMLES strategies to accurately predict the preferential concentration of particles in a channel flow. To the authors' knowledge, this is the first investigation that explores WMLES for particle-laden turbulence and identifies important requirements of the wall model to predict the near-wall transport of inertial particles. This is in contrast to earlier studies that have been devoted to WRLES of particle-laden flows (Kuerten 2016; Marchioli 2017).

The rest of the report is organized as follows. A description of the computational setup and closure problem arising in WMLES of particle-laden turbulence is provided in Section 2. In Section 3, the effect of the missing small scales and the performance of existing particle SGS models are assessed. In Section 4, additional challenges encountered due to the coarse near-wall resolution are discussed and perspectives toward a predictive particle wall-model strategy are analyzed. Section 5 contains concluding remarks and suggestions for future work.

## 2. Computational setup

The transport of inertial point particles in a planar channel flow is computed using the algorithm described in Esmaily *et al.* (2018). It is a finite-volume staggered solver that employs second-order finite-differencing schemes in space, and a second-order Runge-Kutta time-advancement scheme.

The DNS results are obtained by solving the incompressible Navier-Stokes equations subject to periodic boundary conditions in the streamwise  $x_1 = x$  and spanwise  $x_3 = z$  directions, and no-slip no-penetration at the walls in the  $x_2 = y$  direction. A body force in the form of a constant pressure gradient is added to the Navier-Stokes equations in the streamwise direction in order to sustain a statistically steady turbulence characterized by a friction-based Reynolds number  $Re_\tau = u_\tau H / \nu = 600$ . In the notation,  $u_\tau = \sqrt{\tau_w / \rho}$  denotes the friction velocity defined with the wall-shear stress  $\tau_w$  and fluid density  $\rho$ ,  $H$  is the channel half-height, and  $\nu$  is the dynamic viscosity. The total size of the domain is  $4\pi H \times 2H \times 2\pi H$ . The DNS solutions use a uniform grid spacing in the streamwise and spanwise directions, corresponding to 682 and 512 points yielding a grid resolution  $\Delta_1^+ = 11$  and  $\Delta_3^+ = 7.4$ , respectively. The superscripts  $(\cdot)^+$  correspond to quantities non-dimensionalized by the viscous length  $\delta_\nu = \nu / u_\tau$ . In the wall-normal resolution, a stretched mesh is employed that uses 342 grid points. The wall-normal resolution smoothly varies from  $\Delta_2^+ = 0.52$  in the first cell to  $\Delta_2^+ = 7.3$  in the core of the channel.

The WMLES results employ nearly three orders of magnitude fewer grid points uniformly spaced in all directions: 128, 20, and 96 grid points are employed in the streamwise, wall-normal, and spanwise directions. The resulting coarse grid resolutions correspond to  $\Delta_1^+ = 59$ ,  $\Delta_2^+ = 60$ , and  $\Delta_3^+ = 39$ . The large value of  $\Delta_2^+$  corresponds to a resolution in terms of outer units  $\Delta_2 / H = 0.1$ . These WMLES solutions are obtained by solving the filtered Navier-Stokes equations, which describe the conservation of mass and momentum

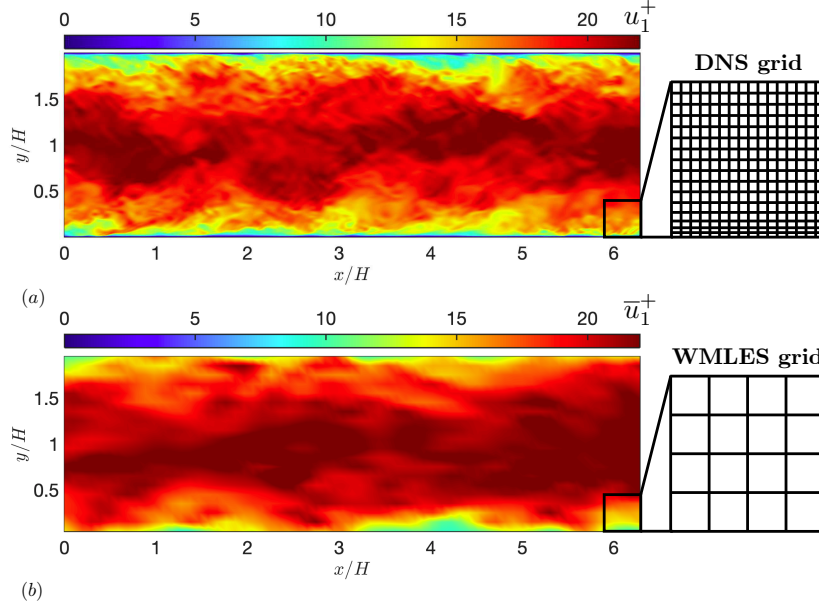


FIGURE 1. Schematic illustrating a typical (a) DNS stretched mesh and (b) uniform WMLES grid, with corresponding contours of the instantaneous streamwise velocity shown for half the domain length in the streamwise direction.

by

$$\frac{\partial \bar{u}_i}{\partial x_i} = 0, \quad (2.1)$$

and

$$\frac{\partial \bar{u}_i}{\partial t} + \bar{u}_j \frac{\partial \bar{u}_i}{\partial x_j} = -\frac{1}{\rho} \frac{\partial \bar{p}}{\partial x_i} + \nu \frac{\partial^2 \bar{u}_i}{\partial x_j \partial x_j} - \frac{\partial \tau_{ij}^{\text{SGS}}}{\partial x_j} + A \delta_{i,1}. \quad (2.2)$$

Time and spatial coordinates are denoted by  $t$  and  $x_i$ .  $\bar{u}_i$ ,  $\bar{p}$ ,  $\rho$ ,  $\nu$ ,  $A$ , and  $\tau_{ij}^{\text{SGS}} = \overline{u_i u_j} - \bar{u}_i \bar{u}_j$  denote the carrier-phase resolved velocity and pressure, density, kinematic viscosity, imposed acceleration, and SGS stress tensor, respectively. The last term is unclosed since the full-scale velocity  $u_i$ , which is the solution of the unfiltered Navier-Stokes equations, is unknown. The SGS stress tensor is modeled in LES using the dynamic Smagorinsky model (Germano *et al.* 1991), where the dynamic constant is calculated using the least-squares approach of Lilly (1992). In the present WMLES calculations, Eqs. (2.1-2.2) are solved using a no-slip velocity boundary condition at the walls, and an alternative reconstruction of the wall-shear stress is obtained via  $\tau_w = \rho u_\tau^2$ , where the friction velocity  $u_\tau$  is locally estimated using the logarithmic law of the wall applied at the first grid point located at  $y^* = \Delta_2/2$ ,

$$u_{\parallel}(y^*) = u_\tau \left[ \frac{1}{\kappa} \log \left( \frac{y^* u_\tau}{\nu} \right) + B \right], \quad (2.3)$$

where  $\kappa = 0.41$  denotes the von Kármán constant,  $B = 5.2$  is an intercept coefficient, and  $u_{\parallel} = \sqrt{u_1^2 + u_3^2}$  is the magnitude of the wall-parallel velocity (Deardorff 1970; Bose & Park 2018). Equation (2.3) is a nonlinear algebraic equation that is locally solved at each wall-adjacent grid point for the friction velocity  $u_\tau$  using the Newton-Raphson method.

Once the friction velocity is computed, the shear stresses at the wall boundaries are set to  $\tau_{12} = \tau_w \left( u_1 / \sqrt{u_1^2 + u_3^2} \right)$  and  $\tau_{32} = \tau_w \left( u_3 / \sqrt{u_1^2 + u_3^2} \right)$ . Figure 1 shows contours of the instantaneous streamwise velocity. The coarse-grained WMLES velocity captures the large-scale motions and mean flow, but is lacking small-scale features throughout the channel.

LES of particle-laden turbulence require the solution of an additional set of equations for the disperse phase. In particular, Lagrangian descriptions employ a set of equations that are solved for each individual particle. The trajectory equation

$$\frac{dx_{p,i}}{dt} = u_{p,i} \quad (2.4)$$

and the equation of motion

$$\frac{du_{p,i}}{dt} = \frac{u_i(x_p) - u_{p,i}}{t_a} \quad (2.5)$$

describe the rate of change of the particle position  $x_p$  and velocity  $u_p$  along each particle trajectory. The particle characteristic time-scale is  $t_a = (2/9)(\rho_p/\rho)(a^2/\nu)$ , with  $\rho_p$  and  $a$  the particle density and radius, respectively. It is assumed in Eq. (2.5) that the particle radius is smaller than the smallest carrier-phase velocity length scale and that the particle density is much larger than that of the carrier fluid (Maxey & Riley 1983). In dilute regimes when the total mass of the disperse phase is negligible compared to the total mass of the carrier phase, Eq. (2.2) does not need to be modified to account for the momentum two-way coupling term describing the force exerted by the particles on the carrier phase. However, in some scenarios, clustering can influence the negligibility of two-way coupling by modifying the localized mass loading, particularly in the range of wall-bounded flows considered where turbophoresis can lead to accumulation of particles in the near-wall region.

In the present study, particles are seeded initially randomly in kinematic equilibrium with the carrier phase at the start of the simulations. The collection of statistics starts after sufficient time has passed for the concentration profile to become stationary. The results are obtained by time averaging over 100 snapshots uniformly spaced in time over 27 flow-through times. Four classes of particles are used in the present study, characterized by viscous Stokes number  $St^+ = 8$  and  $St^+ = 128$ . The viscous Stokes number is computed as  $St^+ = t_a/t_\nu$ , where  $t_\nu = \nu/u_\tau^2$  is the viscous time-scale. For each Stokes number, two different volume fractions  $\Phi_V = 10^{-6}$  and  $\Phi_V = 10^{-5}$  are employed, which correspond to  $5.2 \times 10^5$  and  $5.2 \times 10^6$  particles, respectively. Although the two-way inter-phase momentum coupling is neglected here, the inter-particle and wall-particle collisions are accounted for using the hard sphere model with a unity restitution coefficient. The particle radius in viscous units is  $a^+ = 0.25$ .

Equation (2.5) highlights a closure problem that arises in LES of particle-laden turbulence. The full-scale turbulent velocity  $u_i(x_p)$  that is required at the particle position is unknown in LES since only the large-scale flow velocity  $\bar{u}_i$  is solved for on the LES computational grid. In the present study, at every substep of the time-advancement scheme, the Eulerian velocity to be interpolated to the particle position is one of four different velocities: (a) the DNS velocity  $u_i$  [denoted as DNS in the set of results presented below], (b) the resolved velocity  $\bar{u}_i$  without any SGS model [denoted as WMLES], (c) the resolved velocity  $\bar{u}_i$  supplemented with a differential-filter approximate-deconvolution-modeled turbulent fluctuation velocity on the LES grid as described by Park *et al.* (2015, 2017) [denoted as WMLES-DF], and (d) the full-scale modeled velocity obtained from the spec-

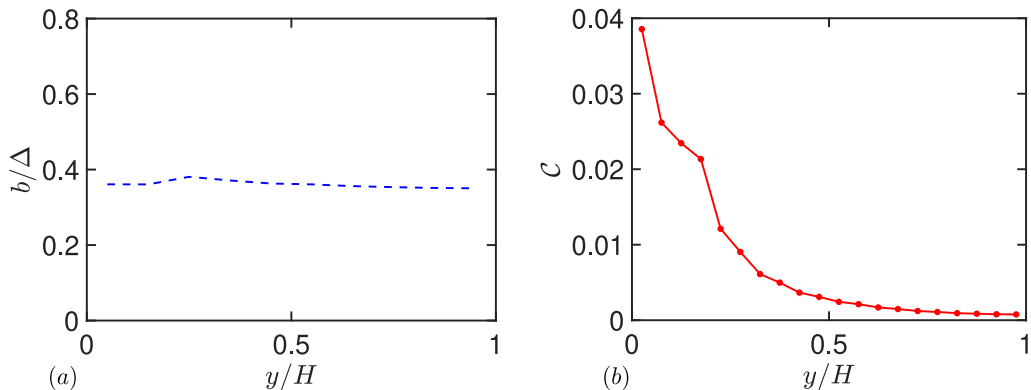


FIGURE 2. Mean profiles of the dynamic coefficients (a)  $b$  and (b)  $C$  involved in the DF and SDF models.

trally enriched differential-filter model as described by Bassenne *et al.* (2017) [denoted as WMLES-SDF]. In the latter, the level of reconstruction correspond to a single-step reconstruction, which corresponds to recovering a velocity field on a  $256 \times 40 \times 192$  grid that remains much coarser than the DNS grid. The WMLES-DF model used in the present study uses the dynamic procedure based on SGS kinetic-energy matching. The interpolation used in the WMLES-SDF model to obtain a velocity field on a finer grid is a fourth-order Lagrange interpolation. Furthermore, the dynamic procedure in the WMLES-SDF model uses two-dimensional filters. For the DNS and all WMLES simulations, the interpolation from the Eulerian grid to the particle position uses the second-order Lagrange interpolation scheme. This choice, in particular in the first near-wall control volumes, is revisited in Section 4.

### 3. Results

#### 3.1. Carrier-phase statistics

Figure 2 shows the mean profiles of the constants that appear in the formulation of the DF and SDF models. These coefficients are dynamically computed in the simulations, and are allowed to vary as a function of wall-normal distance. The value for the DF dynamic constant  $b$  shown in Figure 2(a) corresponds to an effective filter width of the underlying differential filter used to approximately deconvolve the LES velocity. It is nearly uniform in space and consistent with the values reported earlier in isotropic turbulence (Park *et al.* 2015, 2017; Bassenne *et al.* 2017). By way of contrast, the value of the SDF model constant  $C$  shown in Figure 2(b) corresponds to an estimate of the ratio of kinetic energy between eddies with sizes in the range  $[\Delta, 2\Delta]$  to eddies with sizes in the range  $[2\Delta, 4\Delta]$ , where  $\Delta$  is the LES grid resolution. The SDF dynamic constant exhibits large variations in space. In particular, it reaches a maximum at the first grid point around 0.04 and decreases close to 0 as the wall-normal distance increases. The maximum value near the wall is about one-tenth as large as the range of values observed in isotropic turbulence. This warrants further investigation. Unphysical variations are observed in the profile at the first four points near the wall. It is hypothesized that these may be related to wall-modeling errors that manifest themselves in the form of a slight

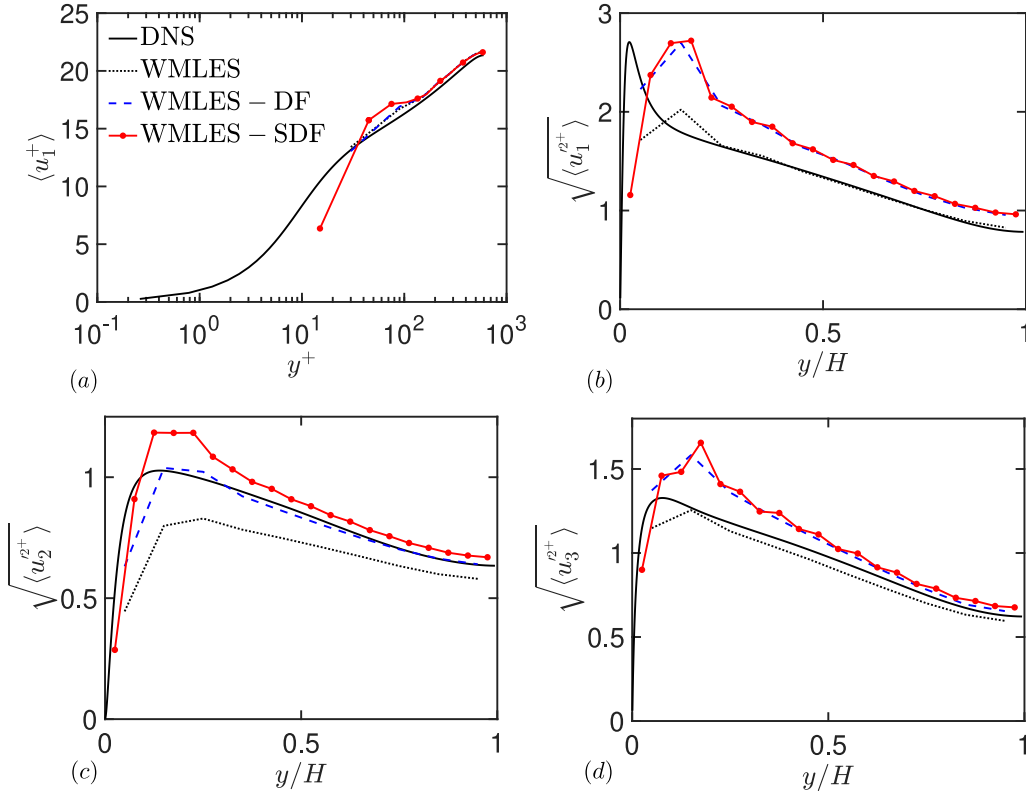


FIGURE 3. (a) Mean streamwise velocity and the (b) streamwise, (c) wall-normal, and (d) spanwise turbulence intensities. The curves correspond to DNS, WMLES, WMLES-DF, and WMLES-SDF.

kink in the first two WMLES grid points in the mean streamwise velocity profile. The two corresponding control volumes contain the first four grid points on the WMLES-SDF grid, thus suggesting that decreasing the flow wall-modeling error would alleviate the kink in the mean profile of  $\mathcal{C}$ .

Figure 3 shows the comparison of the mean streamwise velocity and turbulence intensities. The WMLES solution yields very good agreement with DNS for the mean streamwise velocity and the streamwise and spanwise turbulence intensities, except at the first two grid points, where the profiles are most influenced by wall-modeling errors. However, the wall-normal turbulence intensities are underpredicted. Figure 3 also shows the effect of the SGS models on the Eulerian flow velocity. Note that the SGS models employed in the present study are solely used for integrating the particle equation of motion, and are not used to integrate the equations of the carrier phase. In addition to validating the flow wall model employed in the study, Figure 3 serves as a reference for understanding how the velocity field through which particles are transported is affected by the different SGS modeling strategies. The WMLES-DF profile of the mean streamwise velocity is not significantly changed compared to that of WMLES, unlike the WMLES-SDF profile, which deviates most when closer to the wall. Modeling errors lead to underprediction of the mean at the first grid point and overprediction at the adjacent ones. The addition

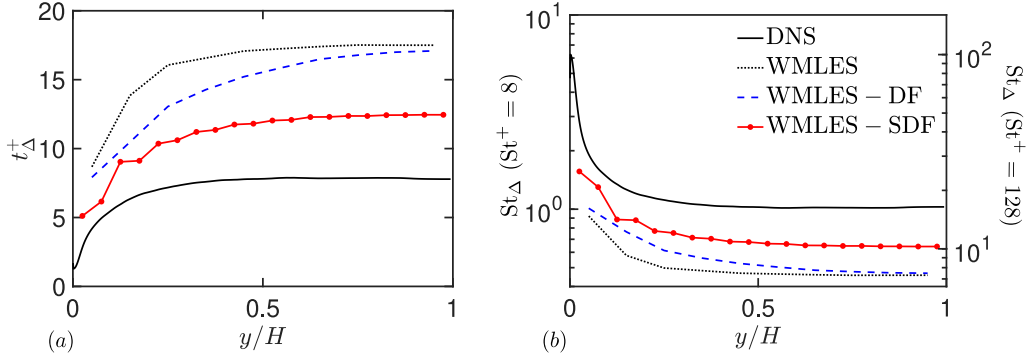


FIGURE 4. Mean profiles of (a) the smallest eddy turnover time and (b) the corresponding Stokes number. The two vertical axes in (b) correspond to viscous Stokes number 8 (left) and 128 (right). The curves correspond to DNS, WMLES, WMLES-DF, and WMLES-SDF.

of the DF and SDF models corresponds to enhancing the turbulence intensities. When the turbulence intensity is already well predicted without any model, as in Figure 3(b,d), the addition of the models leads to overprediction of the intensities. When the intensities are originally underpredicted, the prediction improves. The spectral enrichment in the SDF model does not affect the streamwise and spanwise intensities, and the most noticeable difference is observed in the wall-normal intensity profile in Figure 3(c). Note that even when the total intensities are well predicted in WMLES, the spectral characteristics of that energy might be inaccurate, as the energy might be overestimated in the large wave-number range. In such a scenario, the role of an SGS model would be not only to add SGS energy but also to appropriately redistribute the energy from the large resolved scales to the modeled SGS.

A quantity of particular interest related to the preferential concentration of particles is the SGS Stokes number  $St_\Delta = t_a/t_\Delta$ , where  $t_\Delta$  is the time-scale of eddies of sizes comparable to the grid size (Urzay *et al.* 2014). At any wall-normal location, it can be estimated as  $t_\Delta = \langle 1/\sqrt{S_{ij}S_{ij}} \rangle$ , where  $S_{ij}$  is the strain-rate tensor of the Eulerian velocity used for transporting the particles in each case, and  $\langle \cdot \rangle$  corresponds to averaging along homogeneous spatial directions and time. In the DNS case,  $t_\Delta$  and  $St_\Delta$  correspond to the Kolmogorov time-scale and Stokes number, respectively. Figure 4 shows the mean profile of the time-scale  $t_\Delta$  and Stokes number  $St_\Delta$ . In DNS, the Kolmogorov time scale does not vary throughout most of the channel, and drops near the wall to yield values of the order of the local viscous time scale. The SGS time scale is overpredicted throughout the channel height in WMLES due to the less intense velocity gradients encountered in the coarse calculations. Addition of the DF and SDF models decreases the effective timescales closer to the DNS (Kolmogorov) time-scale throughout the channel as a result of increased gradient intensities. In turn it is possible to estimate the SGS Stokes number, shown in Figure 4(b). In DNS, the local Stokes number varies from 8 (128) at the wall to order 1 (10) in the center of the channel for  $St^+ = 8$  (128) particles. The range of these variations explains some of the discrepancies are analyzed in Section 4.

### 3.2. Dispersed-phase statistics

The spatial distribution of particles is first analyzed by investigating the mean particle number density as a function of wall-normal distance. Figure 5 shows the ratio of the

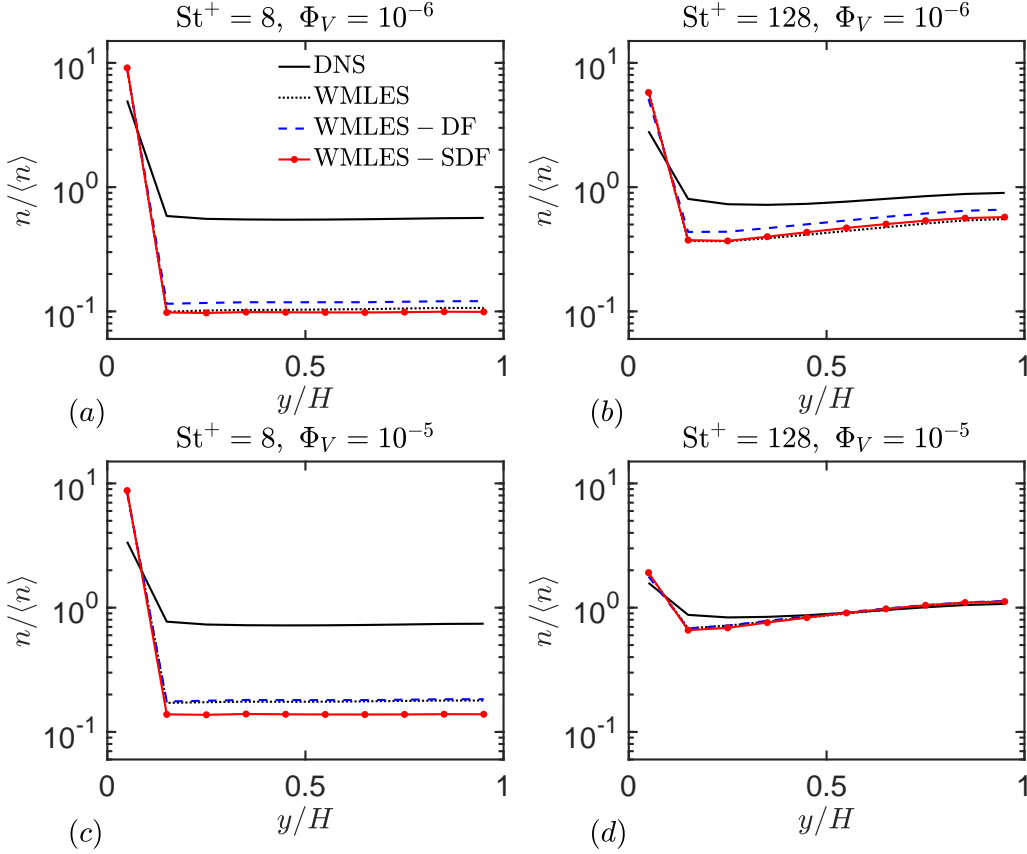


FIGURE 5. Mean particle concentration sampled on the WMLES mesh normalized by the volumetric mean for particles with viscous Stokes number  $St^+ = 8$  (a,c) and  $St^+ = 128$  (b,d). Panels (a,b) correspond to mean volume fraction  $\Phi_V = 10^{-6}$  and panels (c,d) correspond to mean volume fraction  $\Phi_V = 10^{-5}$ . The curves correspond to DNS, WMLES, WMLES-DF, and WMLES-SDF.

number of particles found in a slab at a given distance from the wall divided by the number of particles that would be expected if the particles were randomly distributed in the volume. The particle number density is sampled on the baseline WMLES mesh in order to assess whether the large-scale fluctuations of the number density are resolved on the coarse computational mesh. In DNS the particles are observed to accumulate at the wall where five (three) times as many particles are contained below  $\Delta_2/H = 0.1$  for  $St^+ = 8$  (128) particles, at the lowest volume fraction. This is a result of the turbophoresis phenomenon by which particles tend to migrate toward regions of lower turbulence intensity (Caporaloni *et al.* 1975; Reeks 1983; Johnson 2018). The turbophoretic effect decreases with increasing volume fraction due to the increased number of collisions between particles. In all cases, WMLES overpredicts the near-wall accumulation of particles. In particular at the lowest volume fraction, it predicts twice as many particles in the first layer of control volumes as what is found in DNS for both Stokes numbers. At the lowest Stokes number, it results in an underprediction by a factor of 10 throughout the rest of

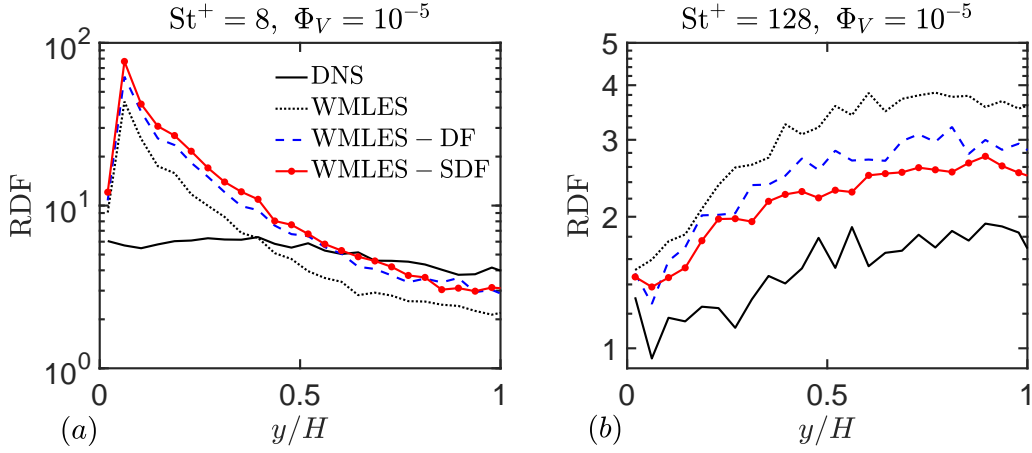


FIGURE 6. Mean particle radial distribution integrated for radial values  $0 \leq r^+ \leq 10$  versus wall-normal distance for particles with viscous Stokes number (a)  $St^+ = 8$  and (b)  $St^+ = 128$  at mean volume fraction  $\Phi_V = 10^{-5}$ . The curves correspond to DNS, WMLES, WMLES-DF, and WMLES-SDF.

the layers. The mismatch between DNS and WMLES is reduced with increasing Stokes number and volume fraction. The former is explained by the decreased turbophoretic effect at larger Stokes number, while the latter is due to the addition of collisional effects that start competing with the hydrodynamic effects, thereby overcoming the effect of the missing hydrodynamic scales. The addition of the particle SGS models does not significantly impact the concentration profiles. Slight improvement is observed for  $St^+ = 8$  particles in the WMLES-DF case, while no improvement or a small adverse effect is observed for  $St^+ = 8$  particles in the WMLES-SDF case. A discussion about a different modeling strategy to improve the prediction of the particle concentration profiles is provided in Section 4.

The preferential concentration of particles is characterized not only by where particles are in the channel but also by how their positions are spatially correlated. In order to assess this aspect of particle clustering, radial distribution functions (RDFs) are computed in slabs of wall-normal thickness  $25\delta_\nu$  at evenly spaced wall-normal locations. The RDF quantifies the likelihood that a given pair of particles is separated by a certain radial distance normalized by that of a random distribution of particles; see, e.g., Ray & Collins (2011) for details. To obtain a compact representation as a function of the wall-normal distance, it is integrated over small radial distances  $0 \leq r^+ \leq 10$ . The results are shown in Figure 6 for the highest volume fraction  $\Phi_V = 10^{-5}$ . In interpreting the results, it is useful to refer to the analysis that followed from Figure 4. In Figure 6(b), particle clustering is shown to slightly increase with increasing wall-normal distance in DNS, consistently with the variation in local Stokes number decreasing from order 100 to order 10 in the center of the channel. In this regime, the WMLES solution overpredicts clustering at all wall-normal locations since at these high values of Stokes numbers small scales act to disperse the particles. The prediction of clustering is improved with addition of the DF and SDF models, although the recovery of the DNS levels is insufficient in the WMLES-SDF case, perhaps due to the use of a single reconstruction level. In Figure 6(a), the WMLES solution underpredicts clustering far from the wall and overpredicts it closer

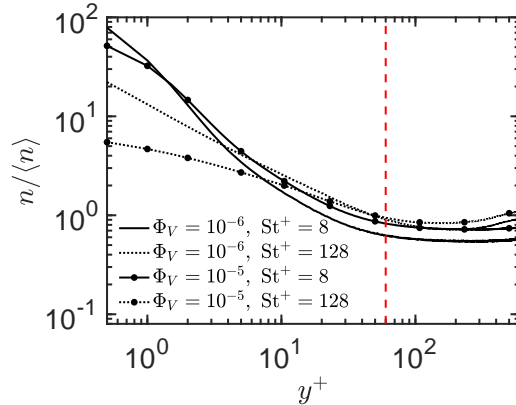


FIGURE 7. Mean particle concentration sampled on a uniform mesh with spacing  $\delta_\nu/2$  normalized by the volumetric mean for particles with viscous Stokes number  $St^+=8$  and  $St^+=128$  and mean volume fractions  $\Phi_V = 10^{-6}$  and  $\Phi_V = 10^{-5}$ . All curves correspond to DNS. The vertical dashed line corresponds to the height of the first control volume in WMLES.

to the wall. Interestingly, this is reasonably consistent with the larger-than-unity values of the local Stokes number closer to the wall, and order-unity values of the Stokes number further away from the wall. Contrary to the largest Stokes number case, at this lower Stokes number, the physical regime of interaction between the particles and the SGS flow motion transitions throughout the channel. This is the first time the DF and SDF models have been employed in wall-bounded turbulence. Note that the behavior follows that observed in isotropic turbulence (Park *et al.* 2015, 2017; Bassenne *et al.* 2017), except at the low Stokes number closer to the wall, where the interaction of particles with near-wall flow structures becomes important.

#### 4. Further considerations on wall-model requirements for particle-laden flows

In this section, the inaccurate predictions of the particle concentration profile in WMLES discussed in Section 3 are addressed in more detail. Figure 7 shows the DNS profiles of the concentration fields sampled on a fine uniform grid with wall-normal spacing equal to half a viscous length in logarithmic scales, along with the corresponding height of the first layer of control volumes in WMLES. This representation of the concentration profile emphasizes the strong accumulation of particles very close to the wall, since the ratio of near-wall to core concentration of particles is nearly two orders of magnitude. Furthermore it shows that the gradients in the concentration profiles are mostly contained within the first control volume in WMLES, rendering the prediction of this quantity extremely challenging in regimes where the SGS flow structures in the first cell play an important role in describing the concentration profile. In particular, a recent analysis by Johnson (2018) reveals that the concentration profile is the result of the competition between the biased sampling of flow structures and the turbophoretic effect [see, e.g., Eq. (2.12) in Johnson (2018)]. The first effect is related to the tendency of inertial particles to accumulate in low-speed streaks associated with ejection events (Eaton & Fessler 1994; Marchioli & Soldati 2002). The second effect is related to particles drifting down to regions of lower turbulence intensity (Caporaloni *et al.* 1975; Reeks 1983; Johnson 2018). The first effect vanishes at high Stokes number and is inherently the result of particle interaction with

near-wall flow structures. By contrast, the second term is a function of the gradient in wall-normal turbulence intensity in the near-wall region regardless of how exactly the particles sample it.

In an attempt to improve the prediction of particle concentration profiles in WMLES, a particle wall-modeling strategy is proposed that consists of adapting the interpolation kernel used in the first near-wall layer of control volumes. In this section, the SGS models discussed in the previous section are deactivated in order to isolate the effect of the interpolation kernel. The baseline case, as described in previous sections, consists of using a traditional second-order Lagrange interpolation kernel everywhere in the channel. Two additional cases are additionally considered. The first, denoted as WMLES –  $\mathcal{I}_{\parallel}$ , consists of employing a different interpolation kernel for the wall-parallel velocity components below the first wall-adjacent grid points. The modified interpolation uses the law of the wall for the mean velocity described by Liakopoulos (1984). The second, denoted as WMLES –  $\mathcal{I}_{\parallel}, \mathcal{I}_{\perp}$ , consists of additionally employing a different interpolating kernel for the wall-normal velocity in the first layer in the following manner. For the wall-normal velocity, the strategy followed here as a first approximation to the problem consists of expressing it as

$$\frac{\bar{u}_2(y)}{\bar{u}_2(\Delta_2^+)} = \frac{\langle \sqrt{u_2'^2} \rangle(y^+)}{\langle \sqrt{u_2'^2} \rangle(\Delta_2^+)} = F(y^+) \quad (4.1)$$

at a given  $y$  location below the first grid point  $\Delta_2$ , where local instantaneous scaling is used to compute the dimensionless quantities. In the expression above, the right-hand side corresponds to the normalized mean profile of the expected standard deviation of the wall-normal velocity. It only depends on the wall-normal coordinate normalized by the viscous length scale. In the present study, it is parameterized using the DNS data as  $F(y^+) = \sum_{k=0}^{k=6} c_k y^{+k}$ , with  $c_0 = -5.0174$ ,  $c_1 = 2.1647$ ,  $c_2 = -0.1280$ ,  $c_3 = -0.01604$ ,  $c_4 = -0.0119$ ,  $c_5 = 0.0033$ , and  $c_6 = -0.0002$ . These parameters yield a fit with a 0.9% relative error with respect to the exact DNS profile of the wall-normal velocity standard deviation. This wall-modeling strategy enforces the right profile of the sampled wall-normal velocity intensity when the first grid value is correctly predicted. This second choice of the interpolation is motivated by the analysis of Johnson (2018), as discussed above, which highlights the role played by this quantity in predicting particle mean concentration profiles. Note that in its current stage, the proposed wall-modeling strategy is not fully predictive since it uses fitted DNS data. The results presented below are obtained from *a posteriori* WMLES calculations. The objective is to assess if this approach is viable, in which case it would motivate the pursuit of predictive wall models for this required quantity in the first cell, unlike conventional wall models that only provide access to the mean streamwise velocity profile.

Figure 8 shows the mean streamwise velocity and turbulence intensities seen by particles in the Lagrangian frame. The conclusions do not vary significantly based on the choice of particle case. The figure uses  $St^+ = 128$  and  $\Phi_V = 10^{-5}$ . Note that the effect of the interpolating kernel is most noticeable below the first grid point of the corresponding velocity component. Outside of the first cell, all curves collapse and oscillate around the Eulerian values shown in Figure 3. The oscillations are due to the use of a second-order Lagrange interpolation. When particles cross the boundary of a cell, they experience a discontinuity in the first derivative of the velocity, which is signified by the oscillations depicted in Figure 8(b-d). The use of a higher-order interpolation scheme with a larger stencil would alleviate these unphysical oscillations. Note also that these results suggest

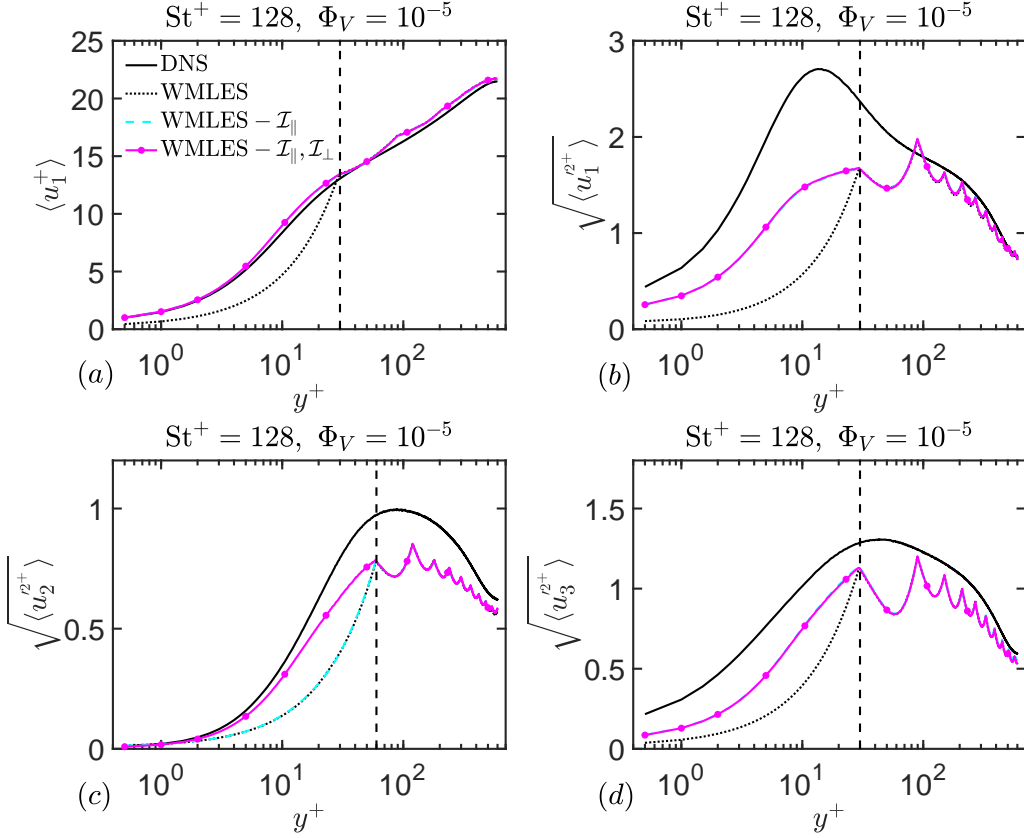


FIGURE 8. (a) Mean streamwise velocity and the (b) streamwise, (c) wall-normal, and (d) spanwise turbulence intensities along particle trajectories for particles with  $St^+ = 128$  and  $\Phi_V = 10^{-5}$ . In each panel, the comparison includes DNS and WMLES with a different choice of first-cell interpolation kernel.

that outside of the first cell, the predictability of the fluid velocity statistics seen by the particles heavily depends on the accuracy of the WMLES solution to capture the mean and intensities on the Eulerian grids, or on the use of a particle SGS model that would enhance these fluctuations to levels corresponding to those observed in DNS, as discussed in Section 3. In particular, the prediction at the first grid point is critical to the prediction within the first cell, in addition to the right choice of the interpolation kernel, since the first off-wall grid point value acts as a matching point for the Lagrangian velocity profile in the first cell.

When no specific choice of interpolation kernel is made and a second-order Lagrange interpolation is applied everywhere, all profiles are significantly underpredicted even in cases where the first grid point value of the corresponding profile is accurately predicted. This highlights the inaccurate continuous representation of the flow statistics implied by this choice of the interpolation kernel in the first cell. Due to the coarse near-wall resolution, the gradients and physics embedded there are significant, and the piecewise trilinear profile obtained with the second-order Lagrange interpolation is a crude approximation. By contrast, the results are improved for the streamwise and spanwise velocities when the

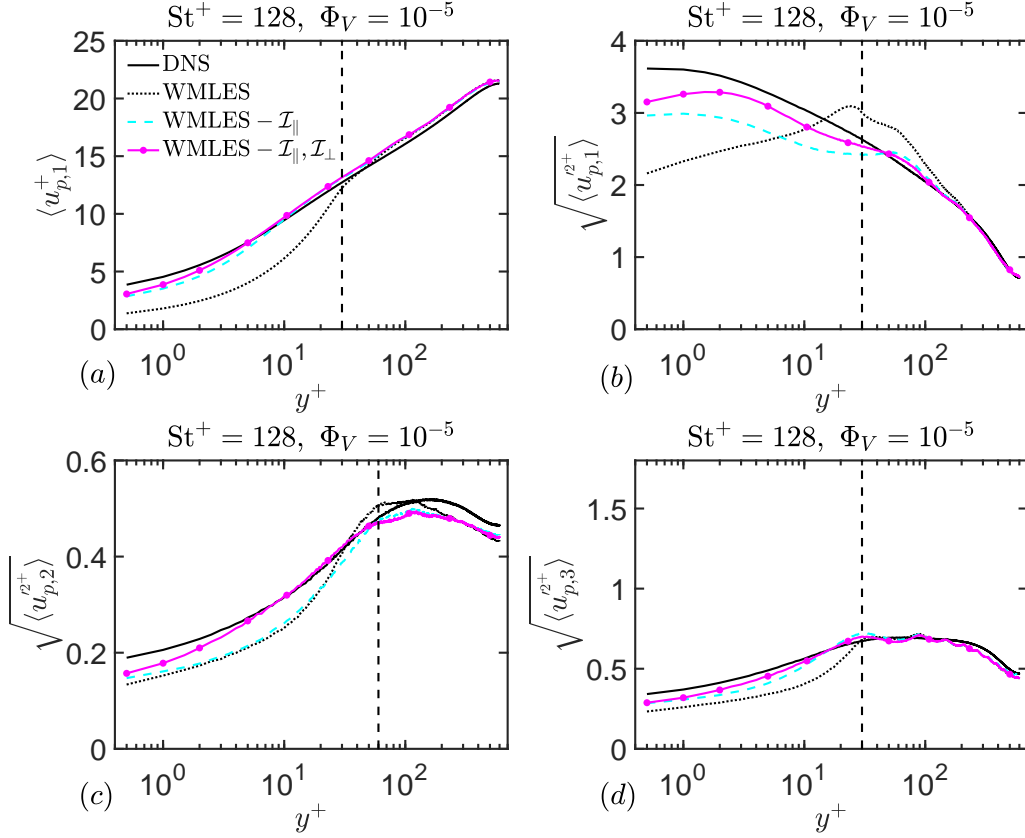


FIGURE 9. (a) Mean streamwise velocity and the (b) streamwise, (c) wall-normal, and (d) spanwise intensities of the particle for particles with  $St^+ = 128$  and  $\Phi_V = 10^{-5}$ . In each panel, the comparison includes DNS and WMLES with different a choice of first-cell interpolation kernel.

law of the wall is used for interpolating the wall-parallel velocity. The shapes of the profile more closely resemble those obtained in DNS, although discrepancies remain partly due to WMLES errors at the first grid point. The wall-normal turbulence intensities are significantly improved by using  $\mathcal{I}_\perp$ , described in Eq. (4.1), suggesting that wall-modeled interpolation kernels for both parallel and perpendicular velocity components are jointly required.

It is instructive to analyze the impact of the improved agreement observed in the WMLES  $-\mathcal{I}_\parallel$  and WMLES  $-\mathcal{I}_\parallel, \mathcal{I}_\perp$  cases with DNS on the particle velocity statistics themselves, as shown in Figure 9. Most of the conclusions drawn above for the fluid velocity sampled by particles translate into similar conclusions for the particle velocity itself. The spurious oscillations observed in Figure 8 are damped since the  $St^+ = 128$  particles acts as low-pass filters and have larger correlation time-scales as they filter the temporal fluctuations along their trajectories. In particular, the profile of the wall-normal velocity fluctuations is very well predicted when the improved interpolation kernel is used for the wall-normal velocity component. Note that this profile is expected to have important consequences on the subsequent concentration profiles, particularly at high Stokes num-

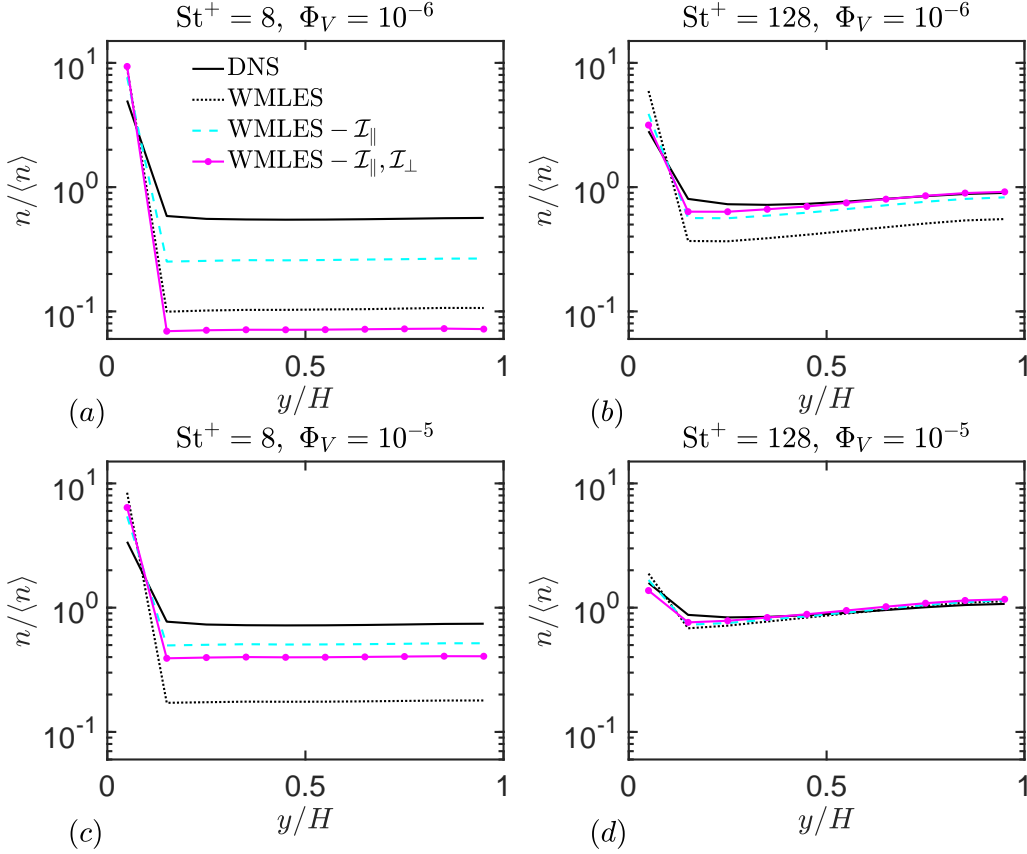


FIGURE 10. Mean particle concentration normalized by the volumetric mean for particles with viscous Stokes number  $St^+ = 8$  (a,c) and  $St^+ = 128$  (b,d). Panels (a,b) correspond to mean volume fraction  $\Phi_V = 10^{-6}$  and panels (c,d) corresponds to mean volume fraction  $\Phi_V = 10^{-5}$ . The different lines correspond to DNS and WMLES with different choices of interpolation kernels in the first cell.

ber, where its gradient profile is the primary driver of near-wall particle accumulation. In the low Stokes number limit, the biased sampling effect becomes important, and it may not be sufficient to predict the former. In other words, at small Stokes number, the structures of the SGS velocity becomes important and it is to be expected that the recovery of the mean wall-normal profile becomes insufficient in this regime.

Finally, the effect of improving the prediction of flow and particle Lagrangian velocities on the mean particle concentration profiles is analyzed. Figure 10 shows the particle concentration profiles obtained with the different particle wall-modeling strategies. The concentration profile prediction is improved when the law of the wall is used for the wall-parallel velocity in all cases, while the use of the improved interpolation for the wall-normal velocity only has an effect for the large Stokes number particles. This is consistent with the above explanation that at small Stokes number the small-scale structures matter, while at large values of the Stokes number the amount of fluctuations is the most important physical mechanism for the dispersion of the particles. These results

have important consequences for predictive SGS modeling. The significant improvements observed for  $St^+ = 128$  particles suggest that the main metric of interest to predict the concentration profile is the wall-normal turbulence intensity profile in the first control volume. To this end, replacing the current DNS-fitted profile used in Eq. (4.1) by a predictive model might be a suitable approach for large Stokes number. The predictive modeling at large Stokes number could perhaps consist of locally employing a Reynolds-averaged Navier-Stokes model for the second-order moment of the wall-normal velocity. The goal is to substitute the fit for  $F(y^+)$  in Eq. (4.1) with a dynamically computed functional form. However, in the limit of small Stokes number, the proposed strategy is insufficient, and an alternative approach needs to be found. This is a much more challenging problem, since the structure of the SGS flow plays an important role in this regime.

Additionally, the results highlight that the SGS enrichment of the velocity on the Eulerian grid is a necessary preliminary step to correct results even if perfect interpolation schemes were used below the first grid point, since inaccurate predictions of the Eulerian flow velocity at the first grid point are carried out in the continuum representation of the velocity below. Additionally, the choice of the interpolation has little to no effect on the RDFs outside of the first control volume (result are not shown here for brevity), particularly at large Stokes number.

## 5. Conclusions

Multi-physics applications that require a detailed description of the flow velocity near the solid boundaries put the traditional wall-modeling strategies to the test. Unresolved fluctuations, intensity extrema, and flow structures between a solid boundary and the first wall-adjacent grid point employed in WMLES may play a predominant role in dictating the overall dynamics of the system.

This report presents results of the application of off-the-shelf WMLES numerical modeling strategies to particle-laden turbulent channel flows, as well as prospective pathways for improving their performance. The focus is on the prediction of the spatial distribution statistics of the disperse phase. The prediction of the mean concentration profile is challenging since most of its gradients are contained in the first control volume typically employed in WMLES. Specifically, it is observed that WMLES overpredicts the near-wall accumulation of particles. In order to address this problem, the choice of the continuous representation of the velocity field below the first grid point is of primary importance.

An exploratory non-predictive wall-modeling strategy is described that performs well for large Stokes number. It relies on using interpolation kernels near the wall that mimic the law of the wall for the wall-parallel velocity, and DNS profiles of the fluctuations for the wall-perpendicular velocity. At lower values of the Stokes number, the problem becomes more challenging and requires the modeling of the rich near-wall structures that are missed in WMLES. The prediction of particle clustering is assessed by computing planar radial distributions. Their prediction requires more than simply changing the interpolation kernels in the first cell. It relies on enriching the Eulerian flow velocity with fluctuations on the LES grid or providing scales smaller than the LES grid to capture the spatial correlation between particle positions. Two off-the-shelf particle SGS models recently developed and assessed in isotropic turbulence are readily applied and shown to improve the prediction of preferential concentration, while they have minimal impact on the mean concentration profile.

### Acknowledgments

The authors are grateful to Sanjeeb Bose for useful discussions. This investigation was funded by the Advanced Simulation and Computing (ASC) program of the US Department of Energy's National Nuclear Security Administration via the PSAAP-II Center at Stanford, Grant No. DE-NA0002373.

### REFERENCES

- BASSENNE, M., ESMAILY, M., LIVESCU, D., MOIN, P. & URZAY, J. 2017 Dynamic spectrally-enriched LES subgrid-scale modeling for preferential concentration of inertial particles in turbulence. *Annual Research Briefs*, Center for Turbulence Research, Stanford University, pp. 3–19.
- BOSE, S. T. & PARK, G. I. 2018 Wall-modeled large-eddy simulation for complex turbulent flows. *Annu. Rev. Fluid Mech.* **50**, 535–561.
- CAPORALONI, M., TAMPIERI, F., TROMBETTI, F. & VITTORI, O. 1975 Transfer of particles in nonisotropic air turbulence. *J. Atmos. Sci.* **32**, 565–568.
- CHAPMAN, D. R. 1979 Computational aerodynamics development and outlook. *AIAA J.* **17**, 1293–1313.
- CHOI, H. & MOIN, P. 2012 Grid-point requirements for large eddy simulation: Chapman's estimates revisited. *Phys. Fluids* **24**, 011702.
- DEARDORFF, J. W. 1970 A numerical study of three-dimensional turbulent channel flow at large Reynolds numbers. *J. Fluid Mech.* **41**, 453–480.
- EATON, J. K. & FESSLER, J. R. 1994 Preferential concentration of particles by turbulence. *Int. J. Multiphas. Flow* **20**, 169–209.
- ESMAILY, M., JOFRE, L., MANI, A. & IACCARINO, G. 2018 A scalable geometric multi-grid solver for nonsymmetric elliptic systems with application to variable-density flows. *J. Comput. Phys.* **357**, 142–158.
- GERMANO, M., PIOMELLI, U., MOIN, P. & CABOT, W. 1991 A dynamic subgrid-scale eddy viscosity model. *Phys. Fluids* **3**, 1760–1765.
- JOHNSON, P. & MENEVEAU, C. 2018 Predicting viscous-range velocity gradient dynamics in large-eddy simulations of turbulence. *J. Fluid Mech.* **837**, 80–114.
- JOHNSON, P. L. 2018 Toward wall-modeled LES of particle-laden flows: Analysis of turbophoresis and inter-particle collisions in a turbulent channel flow. *Annual Research Briefs*, Center for Turbulence Research, Stanford University, pp. 111–124.
- KUERTEN, J. G. M. 2016 Point-particle DNS and LES of particle-laden turbulent flow—a state-of-the-art review. *Flow Turbul. Combust.* **97**, 689–713.
- LIAKOPOULOS, A. 1984 Explicit representations of the complete velocity profile in a turbulent boundary layer. *AIAA J.* **22**, 844–846.
- LILLY, D. K. 1992 A proposed modification of the Germano subgrid-scale closure method. *Phys. Fluids* **4**, 633–635.
- MARCHIOLI, C. 2017 Large-eddy simulation of turbulent dispersed flows: a review of modelling approaches. *Acta Mech.* **228**, 741–771.
- MARCHIOLI, C. & SOLDATI, A. 2002 Mechanisms for particle transfer and segregation in a turbulent boundary layer. *J. Fluid Mech.* **468**, 283–315.
- MAXEY, M. R. & RILEY, J. J. 1983 Equation of motion for a small rigid sphere in a nonuniform flow. *Phys. Fluids* **26**, 883–889.

- PARK, G. I., BASSENNE, M., URZAY, J. & MOIN, P. 2017 A simple dynamic subgrid-scale model for LES of particle-laden turbulence. *Phys. Rev. Fluids* **2**, 044301.
- PARK, G. I., URZAY, J., BASSENNE, M. & MOIN, P. 2015 A dynamic subgrid-scale model based on differential filters for LES of particle-laden turbulent flows. *Annual Research Briefs*, Center for Turbulence Research, Stanford University, pp. 17–26.
- RAY, B. & COLLINS, L. 2011 Preferential concentration and relative velocity statistics of inertial particles in Navier-Stokes turbulence with and without filtering. *J. Fluid Mech.* **680**, 488–510.
- REEKS, M. W. 1983 The transport of discrete particles in inhomogeneous turbulence. *J. Aerosol Sci.* **14**, 729–739.
- SAGAUT, P. 2006 *Large Eddy Simulation for Incompressible Flows: An Introduction*. Springer.
- URZAY, J., BASSENNE, M., PARK, G. I. & MOIN, P. 2014 Characteristic regimes of subgrid-scale coupling in LES of particle-laden turbulent flows. *Annual Research Briefs*, Center for Turbulence Research, Stanford University, pp. 3–13.